




Evidence of twinning-induced plasticity (TWIP) and ultrahigh hardness in additively-manufactured near-eutectic Ni–Nb

Morgan R. Jones^{1,2}, N. Scott Bobbitt², Frank W. DelRio², Mark A. Wilson², Hannah C. Howard¹, Melina A. Endsley¹, Jonathan W. Pegues², Ping Lu², Andrew B. Kustas², Irene J. Beyerlein¹, Michael Chandross², and Nicolas Argibay^{3,*} 

¹ Materials Department, University of California, Santa Barbara, Santa Barbara, CA 93106, USA

² Material, Physical, and Chemical Sciences Center, Sandia National Laboratories, Albuquerque, NM 87123, USA

³ Division of Materials Sciences and Engineering, Ames National Laboratory, Ames, IA 50011, USA

Received: 3 April 2023

Accepted: 24 May 2023

Published online:

7 June 2023

© The Author(s), under exclusive licence to Springer Science+Business Media, LLC, part of Springer Nature 2023

ABSTRACT

The temperature-dependent hardness of additively-manufactured near-eutectic Ni–Nb was investigated. This alloy was found to have solidified into a two-phase nanoscale microstructure with peak hardness of $H \cong 14\text{--}17$ GPa at temperatures up to 400 °C, above which irreversible softening was observed despite retention of significant strength compared to traditionally-synthesized Ni-based superalloys. Experiments and molecular-dynamics simulations show that deformation for single-phase nanocrystalline volumes was confined to intragranular slip-band formation in $\delta\text{-Ni}_3\text{Nb}$ and to intergranular grain-boundary sliding in $\mu\text{-Ni}_6\text{Nb}_7$. However, microscopy in the nanostructured two-phase regions after severe plastic deformation indicated that phase boundaries acted as nucleation sites for dislocations, promoting twinning-induced plasticity (TWIP) in the $\mu\text{-Ni}_6\text{Nb}_7$ grains. This work highlights (1) that additive manufacturing techniques enable formation of unique microstructures that exhibit superior mechanical properties, and (2) that multi-phase intermetallic compounds provide a route to mitigate brittle fracture through the promotion of twinning-induced plasticity. High strength and the absence of interface decohesion (cracking) suggests that multi-phase intermetallic systems may be a viable route for design of new printable superalloys. These results suggest that additive manufacturing methods and rapid solidification via non-equilibrium pathways may enable a pathway for achieving high combined strength and ductility.

Handling Editor: Megumi Kawasaki.

Address correspondence to E-mail: nargibay@ameslab.gov

<https://doi.org/10.1007/s10853-023-08636-8>

Introduction

Alloy research is driven by the need for structural materials that can survive increasingly harsh operating conditions. Gas turbines are one example application where energy efficiency, reliability, and safety are limited by a material resistance to prolonged exposure to high temperatures and stresses. Ni-based superalloys have been a successful commercial solution in this space [1]. The development of new superalloys or alternatives to superalloys has involved microstructural engineering [1]. Additive manufacturing (AM) techniques have been shown to produce microstructures with advantageous properties, including pathways for overcoming ductility challenges in historically-brittle alloys that are otherwise difficult or impossible to achieve with traditional fabrication methods (e.g., casting, deformation processing) [2–7]. Examples of desirable deformation mechanisms in high-strength materials, where cohesive failure is often energetically favorable compared to intragranular deformation, include transformation-induced plasticity/twinning-induced plasticity (TRIP/TWIP), as has been shown in some steels [8, 9] and high-entropy alloys [10]. In these materials, a combination of high strength and ductility is achieved through deformation twinning, where twins accommodate deformation while at the same time impeding dislocation motion and accumulation [11–13].

Here, we show that AM fabrication of the near-eutectic Ni–Nb binary alloy resulted in the formation of a dual-phase intermetallic δ -Ni₃Nb/ μ -Ni₆Nb₇ microstructure. Although intermetallic compounds are conventionally considered intrinsically brittle and thus of limited practical utility, several recent studies have shown that multi-phase intermetallics can be tailored to produce both high hardness and ductility [14–16]. For example, in the Ti–Al dual-phase system, it was found that ductility increased with decreasing grain size [17, 18], a trend not commonly seen in pure metals. Additionally, there have been investigations of multi-principal-element alloys which possess lamellar, dual-phase intermetallic microstructures that preferentially undergo deformation twinning [19, 20]. Both the δ and μ intermetallic phases have also received attention due to (1) their presence in Ni-based superalloys and (2) their role in imparting high strength as precipitate phases. For example, in

Inconel 718 and 625 the δ structure has been shown to improve stress-rupture ductility [21], increase fatigue resistance (by hindering dislocation glide [22]), slow grain coarsening [23], and delay recrystallization [23]. The less common μ phase could be promising for use in high-temperature structural materials due to its high melting temperature, strength, and creep resistance [24, 25]. However, its processability is limited by brittleness, even at high homologous temperatures [24]. Here, we present evidence that fracture mitigation is possible through additive manufacturing by promoting plastic deformation modes that can impart some ductility to otherwise brittle compounds.

Previously [26], we presented Ni_{59.5}Nb_{40.5} fabricated by AM and reported its impressive combination of high hardness, $H = 14\text{--}17$ GPa and fracture toughness. These hardness values exceed those reported for most nanocrystalline metals, multi-principal-element alloys, and superalloys [27–32]. We showed that this material possesses a cellular, multimodal microstructure with two phases: nanoscale δ -Ni₃Nb precipitates in a μ -Ni₆Nb₇ matrix phase. Here, we investigate the phase-dependent deformation mechanisms in this material using ambient and high-temperature nanoindentation, electron microscopy for microstructure characterization, and molecular dynamics simulations. TWIP was observed and attributed to the presence of the phase boundaries, associated with a nanoscale cellular structure. It is thus demonstrated that AM fabrication can produce microstructures that promote deformation twinning in traditionally brittle intermetallics, giving rise to favorable mechanical properties (i.e., high strength and good ductility).

Methods

Fabrication and processing

A near-eutectic binary Ni–Nb alloy, with a global composition of Ni_{59.5}Nb_{40.5}, was fabricated utilizing an open-architecture laser-beam directed-energy deposition (LB-DED) AM system. Full details of the LB-DED system are available elsewhere [33]. Briefly, it is equipped with a YLS-2000 fiber laser that emits at 1064 nm wavelength, which is mounted to the spindle of a 3-axis Tormach CNC 770 milling machine housed in a glovebox. A continuously purging Ar gas creates an inert environment that typically

maintains < 50 ppm O_2 and < 10 ppm H_2O during AM processing. A pre-blended Ni–Nb powder feedstock was fluidized from a single powder hopper via a rotary feed wheel and Ar carrier gas toward the melt pool for layer-by-layer consolidation. Powder blending was facilitated by pouring the Ni and Nb powders into a bottle that was subsequently placed on a mechanical tumbler. A compact metallurgical sample in the form of a single-pass thin wall was produced with laser power = 500 W, scan velocity = 400 mm/min, layer height = 0.2 mm, and a 1 mm laser spot size; the dimensions were approximately 25 mm (track/specimen length) by 25 mm (specimen height) by ~ 2 –3 mm (a single-bead specimen width). Given the nominal 0.2 mm layer height, the sample consisted of roughly 125 total layers. The substrate was a Ni 200 plate that was maintained at 12 °C via a contact heat exchanger with flowing refrigerated water. A chilled substrate was utilized to maximum layerwise solidification rates and minimize effective part reheating, toward refining the as-built microstructure. Prior to microstructural characterization and testing, the surface of the $Ni_{59.5}Nb_{40.5}$ specimen was polished to an average roughness of $R_a \cong 25$ nm using a 0.3 μm Al_2O_3 and a 0.04 μm SiO_2 slurry.

Nanoindentation

Nanoindentation experiments were performed using a Berkovich tip on a Hysitron TI-980 nanoindenter equipped with a TriboIndenter magnetic sample stage. A detailed overview of the experimental techniques and calibration procedures for room-temperature nanoindentation testing can be found elsewhere [26]. Indentation of a 10×10 sample array was performed on the $Ni_{59.5}Nb_{40.5}$ specimen with a 10 mN maximum load and 10 μm spacing between indents. A constant strain rate CMX (Continuous Measurement of X) load function was employed during testing to elucidate the depth-dependent hardness, H , of each indent. One-way ANOVA and a Tukey's multiple comparisons test [34] were used to determine statistical significance between the hardness values of different regions.

An XSol environmental stage and high-temperature Berkovich tip were utilized for high-temperature nanoindentation experiments. A constant stream of N_2 gas flowed over the sample during testing to minimize oxidation effects. Five indents spaced

10 μm apart were performed at each temperature (25, 200, 400, 600, and 800 °C) using a 10 mN standard trapezoidal load function. Hardness at each temperature point was taken as the average value from the five indents.

Transmission electron microscopy and electron-backscatter diffraction phase identification

Transmission electron microscopy (TEM) specimens in cross-section were extracted from the nano-indented areas by focused ion beam (FIB) methods. An FEI TitanTM G2 80-200 scanning transmission electron microscopy (STEM) with a Cs probe corrector and ChemiSTEMTM technology (X-FEGTM and SuperXTM EDS with four windowless silicon drift detectors) operated at 200 kV was used in this study. The microstructure was examined by STEM using high-angle annular-dark-field (HAADF) and bright-field (BF) detectors. The film composition was studied by STEM energy-dispersive spectroscopy (EDS) spectral imaging acquired as a series of frames where the same region was scanned multiple times. An electron probe of size less than 0.13 nm, convergence angle of 18.1 mrad, and current of ~ 75 pA was used for data acquisition. HAADF and BF images were recorded under similar optical conditions using a detector with a collection range of 60–160 mrad and 0–9 mrad, respectively.

SEM specimens were mounted in cold-set epoxy and ground with a series of SiC paper, followed by polishing with a 1 μm diamond suspension. The sample was then prepped for EBSD analysis using a two-step vibratory polishing procedure utilizing a 0.3 μm Al_2O_3 slurry followed by a 0.04 μm SiO_2 slurry. SEM imaging and EBSD were performed on a Zeiss Supra 55-VP FE-SEM equipped with Symmetry EBSD detectors. EBSD was performed at 20 kV for select regions to determine the grain and phase morphology.

Molecular dynamics

Molecular-dynamics (MD) simulations were performed with LAMMPS [35, 36] (v Oct 29, 2020) using the Finnis–Sinclair potential for Ni–Nb developed by Zhang et al. [37]. This potential was originally fit for liquid and amorphous $Nb_{62}Ni_{38}$ alloys and shows good agreement with ab-initio calculations. Bulk

samples of Ni_3Nb and Ni_6Nb_7 were created with equivalent microstructures, specifically meaning that between systems the grain sizes and relative rotations are identical, but the atomic structure of each material was generated from the appropriate crystalline unit cell according to a CIF file from materialsproject.org. Polycrystalline rods with length and diameter of 500 Å were cut from the bulk crystal and consisted of an average grain size of 13.1 ± 4.4 nm.

Tensile tests were performed by applying a constant velocity of 0.01 Å/ps, parallel to the rod axis, to a fixed region on each end of the rod, approximately 15 Å thick. Prior to straining, structures were minimized and then equilibrated at 300 K for 30 ps in the isothermal, isobaric, and constituent invariant (NPT) ensemble. The strain reported is the percentage of the rod length stretched from its original length (i.e., engineering strain) and stress was computed as the sum of forces in the fixed atoms on either end of the rod in the direction of the tensile strain, divided by the original cross-sectional area of the rod. Flow stress was computed as the average stress from 6 to 10% strain.

The polycrystalline configurations were generated from a mesoscale microstructure created using a Monte Carlo Potts model that accurately represent curvature driven grain growth kinetics [38, 39]. Using the SPPARKS [40] Kinetic Monte Carlo (KMC) code, we started from a discretized configuration of $50 \times 50 \times 50$ on-lattice elements each having a random assignment from 1000 different spin values. The configuration was evolved in time according to rejection-KMC rules, to create a system representative of grains in a polycrystalline microstructure. With sufficient simulation time, the system showed grain coarsening to the point where a single spin value remained. A single snapshot during this time evolution was chosen as our representative discretized configuration, with approximately three to five grains spanning the simulation cell in each direction.

We converted this snapshot to an atomistic representation with a given length-scale for the simulation cell. This dictates the discretized voxel size and grain size in the mesoscale representation. For each unique grain, we determined a bounding polyhedron through the identification of connected neighboring voxels with identical spin values. The polyhedron was filled with atoms from a single crystal (created from replicated unit cells as defined by the CIF files

from materialsproject.org) given a random 3-dimensional crystallographic rotation and then, trimmed to the bounding polyhedron of the given grain. While assuring the preservation of periodic boundary conditions, this process was repeated until all grains were populated. Overlapping atoms (defined as within 1.0 Å of their nearest neighbor) were deleted, and a minimization was performed on the structure to remove non-physical configurations. Notably, each configuration was constructed using an identical random seed. As a result, each configuration has identical microstructure with the same per-grain crystallographic orientation, eliminating potential variability in our results due to microstructural differences or anisotropy.

Results and discussion

Hardness

Figure 1 summarizes the results of nanoindentation measurements on the $\text{Ni}_{59.5}\text{Nb}_{40.5}$ specimen. Hardness is plotted as a function of indentation depth, as shown in Fig. 1A. Regardless of indent location, all hardness values initially skewed toward higher values at shallower penetration depths, before reaching steady-state values at depths greater than approximately 125 nm. This behavior is common with crystalline materials [41–43], and indentation size effects have been shown to accurately describe such behavior [44–46]. At shallow indentation depths, plastic deformation is confined to small volumes, where strain gradients are large and contribute significantly to the flow stress of the crystalline material. Beyond a critical value, indentation measurements become insensitive to depth and converge to the bulk hardness of the sample. With small enough sampling volumes, for example when they are smaller than the grain size or average space between defects, the hardness can be extremely high, converging toward the idealized strength of defect-free metals [47].

Following the series of indentation tests, EBSD was used to generate a contrast image (Fig. 1B) and a phase map (Fig. 1C). As reported in our previous study [26], microstructural analysis of the $\text{Ni}_{59.5}\text{Nb}_{40.5}$ specimen revealed the presence of two distinct intermetallic structures: the orthorhombic (D0_a) $\delta\text{-Ni}_3\text{Nb}$ phase and the rhombohedral ($\text{D}8_3$) $\mu\text{-Ni}_6\text{Nb}_7$ phase. As evidenced in Fig. 1B and C, the

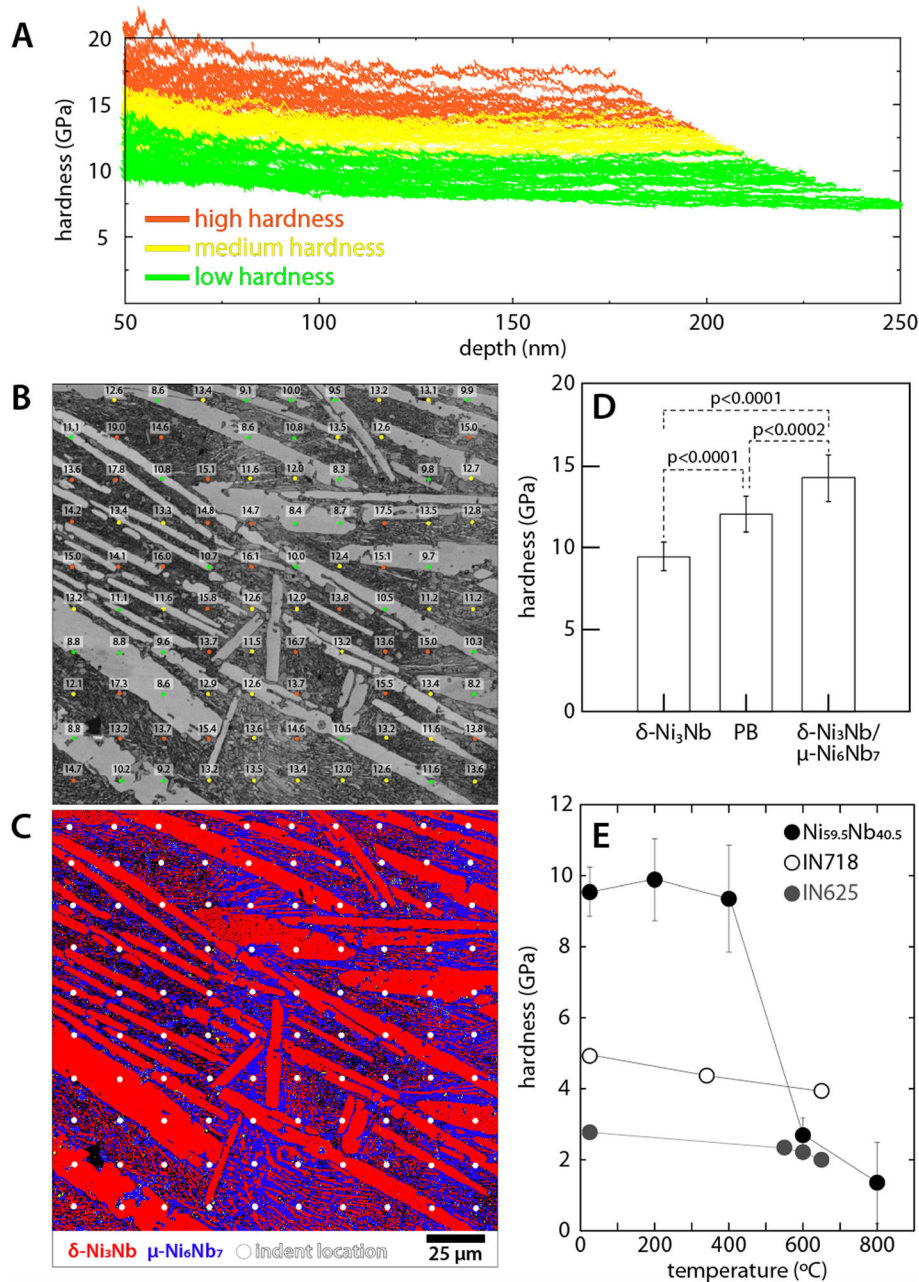


Figure 1 Results of nanoindentation measurements and characterization. **A** Hardness as a function of indentation depth on the AM near-eutectic specimen. Color coding of high, medium, and low hardness corresponds to indent locations shown in **(B)**. **B** Contrast image formed from EBSD pattern quality. Indent locations are overlaid with color coded circles, and average hardness value is shown above each location (in GPa). **C** EBSD phase map with indent locations marked with white circles. Two distinct phases are present, δ -Ni₃Nb and μ -Ni₆Nb₇. **D** Bar graph depicting the hardness of different phase regions. The *p*-value

between each data set is shown above dotted brackets. **E** Temperature-dependent hardness of the near-eutectic Ni_{59.5}Nb_{40.5} specimen assessed via high-temperature nanoindentation. Average hardness values and corresponding error bars were found by computing the average and standard deviation of nanoindentation data sets. Temperature-dependent hardness data of Ni-based superalloys from literature [55, 56] are included to highlight the engineering relevance of the Ni_{59.5}Nb_{40.5} specimen.

microstructure is composed of larger needle-like primary δ -Ni₃Nb grains, dispersed in a dual-phase matrix of finer-grained lamellar (eutectic) δ -Ni₃Nb/ μ -Ni₆Nb₇. Through the combination of nanoindentation and EBSD characterization, we identified regions of high hardness and correlated these regions to specific microstructures and phases.

Average values of steady-state hardness (in units of GPa) are reported above the given indent location in Fig. 1B. Indent locations are overlaid with color coded circles corresponding to high (orange), medium (yellow), or green (low) average hardness values. Upon inspection of Fig. 1B and C, trends emerge in the relationship between hardness and indentation location. Specifically, average hardness values were lower, $H_{\text{avg}} \cong 8$ –12 GPa, for locations within large δ -Ni₃Nb grains, and considerably higher, $H_{\text{avg}} \cong 14$ –17 GPa, within δ -Ni₃Nb/ μ -Ni₆Nb₇ lamellar regions that possessed nanoscale δ -Ni₃Nb phases.

Figure 1D further highlights the region-dependent hardness for large δ -Ni₃Nb grains (left, $H_{\text{avg}} \cong 9.6$ GPa), phase boundaries of the large δ -Ni₃Nb grains (middle, $H_{\text{avg}} \cong 12.6$ GPa), and the dual-phase δ -Ni₃Nb/ μ -Ni₆Nb₇ mixed regions (right, $H_{\text{avg}} \cong 14.2$ GPa). Medium hardness values $H_{\text{avg}} \cong 12$ –14 GPa were generally observed for indent locations on δ -Ni₃Nb phase boundaries or dual-phase regions that possessed larger δ -Ni₃Nb grains within the μ -Ni₆Nb₇ matrix. Because regions of hardness fall within the error bars of other hardness regions in Fig. 1D, a multiple comparisons test was employed to ensure; there was no statistical significance between groups. Probability values (*p*-values), shown for regions of hardness in Fig. 1D, all fall well below 0.05, indicating that average hardness showed negligible correlation between regions.

The formation of large, needle-shaped δ -Ni₃Nb phases have been widely reported in literature for Ni-based superalloys [21, 48, 49], but few studies have been conducted to assess the mechanical properties of this phase [49–51]. These focused on how Ni₃Nb precipitates influenced mechanical properties of Inconel 718 at variable temperatures [49] and on single-crystal deformation mechanisms of the Ni₃Nb phase [50, 51]. Like the present work, it was found that Ni₃Nb precipitates exhibited a needle-like morphology in Inconel 718; at a 40% Ni₃Nb phase fraction, an increase in hardness and fatigue life was reported, though significant embrittlement was

observed above 40%. The single-crystal work focused on compression and tensile testing at variable temperature, concluding that the isolated phase had negligible ductility in tension, but ductile in compression attributed to suppression of {211} twin formation. In contrast, here, we found nearly complete suppression of intragranular deformation in the Ni₃Nb crystallites in the nanostructured two-phase region and shear banding in the coarse grained isolated Ni₃Nb regions. Afonso, et al. [52] reported a hardness value of $H \cong 4.13$ GPa for the irregular coarse grained γ'' -Ni₃Nb phase. These authors identified the δ -Ni₃Nb phase for a rapidly solidified Ni₇₀Nb₃₀ specimen but did not perform Vickers microhardness testing on the individual phase. The study reported a coexistence of δ -Ni₃Nb + γ -Ni in Ni₇₀Nb₃₀ that exhibited an overall hardness value of $H \cong 4.13$ GPa, more than 2× the measured hardness of the individual γ -Ni phase ($H \cong 1.8$ GPa). Our current results show that the average hardness of the δ -Ni₃Nb phase ranged from $H \cong 8.2$ –11.6 GPa, more than 2× the hardness of the γ'' -Ni₃Nb phase reported previously [52]. For traditional fabrication of Ni-based superalloys (e.g., Inconel 718 and Inconel 625), it has been shown that precipitation of the γ'' -Ni₃Nb phase precedes the formation of the (apparently much harder) δ -Ni₃Nb phase [21]. Because of this, post-processing steps, such as heat treatments, are needed to generate the δ structure. With AM techniques, it was possible to evaluate the δ -Ni₃Nb structure without the need for post-fabrication treatments.

Results of temperature-dependent hardness from high-temperature nanoindentation experiments are shown in Fig. 1E. The temperature-dependent hardness behavior of the Ni_{59.5}Nb_{40.5} specimen was evaluated with five indents performed at each temperature. Indents were performed across δ -Ni₃Nb large grains as well as the dual phase δ -Ni₃Nb/ μ -Ni₆Nb₇ region. Tests revealed the Ni_{59.5}Nb_{40.5} sample exhibited a retention in hardness ($H \cong 10$ GPa) up to 400 °C, followed by a sharp drop in hardness ($H \cong 1.5$ –2.5 GPa) at higher temperatures. Although softening was significant, the measured hardness values of Ni_{59.5}Nb_{40.5} at 600 °C and 800 °C were nearly equivalent to reported strengths of Ni-based superalloys at $T > 400$ °C [53]. The melting temperature for this near-eutectic alloy is, $T_{\text{melt}} \cong 1100$ °C [54]. The observed decrease in hardness occurred close to the homologous temperature,

$T_{\text{homologous}} = \frac{T_{\text{test}}}{T_{\text{melt}}} \cong 0.5$, where diffusion processes become dominant in the deformation of the material. Post-anneal hardness of the specimen (Fig. 1E) was $H \cong 3.8\text{--}4.8$ GPa, indicating that exposure to high temperatures during nanoindentation softened the specimen to a level that is commensurate with annealed Ni-based superalloys. The reduction can result from temperature-driven microstructural evolution via phase transformations, recrystallization, grain coarsening, or a decrease in dislocation density.

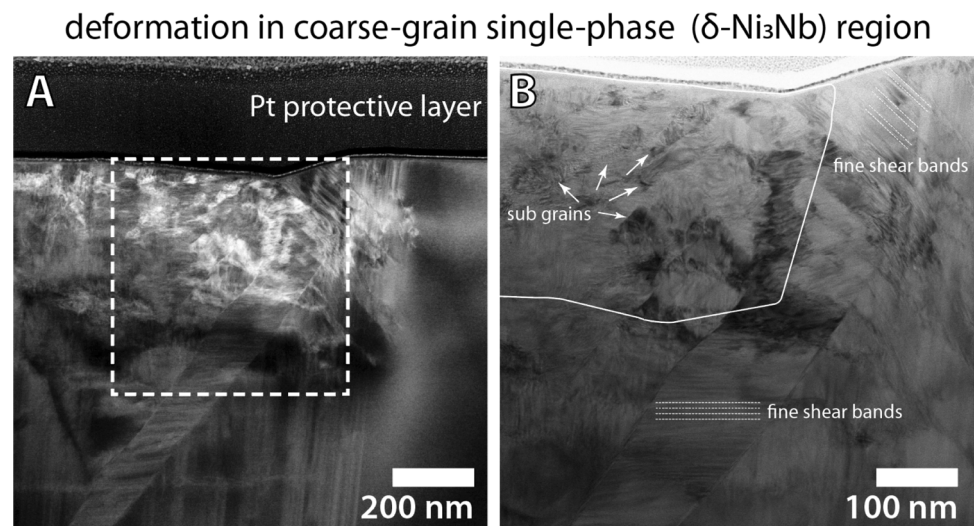
Microstructure and deformation characterization

Cross-sectional STEM images of nanoindentation-induced deformation zones are shown in Fig. 2. Figure 2A and B were generated from FIB-prepared cross-sectional specimens extracted from the center of an indentation site on a large $\delta\text{-Ni}_3\text{Nb}$ grain and within the dual-phase region, respectively. Multiple distinct deformation modes were observed in the single phase $\delta\text{-Ni}_3\text{Nb}$, all associated with severe plastic deformation [57, 58], including extreme grain refinement, sub-grains (measuring 10 s of nm), and fine shear bands near the surface as well as in the bulk. Nanoindentation experiments performed in CMX mode were oscillatory in nature, and other dynamic mechanical testing techniques, such as laser shock processing (LSP) and dynamic plastic deformation (DPD), have also been shown to promote the formation of sub-grain structures and shear bands. LSP studies have shown that the accumulation of dislocation walls was the mechanism responsible for

sub-grain formation in AISI 8620 steel [59] and Ti-6Al-4V [60]. Hong et al. [61] performed an extensive study on the nucleation of fine shear bands (thickness ~ 100 nm–200 nm) in a twinned Cu-Al alloy subjected to DPD and showed the nucleation stage results from highly localized deformation, in which crystal rotation occurs and high shear strains are introduced. The TEM results shown in Fig. 2 for the coarse grained $\delta\text{-Ni}_3\text{Nb}$ subjected to dynamic indentation loading suggest that plasticity was accommodated by (1) formation of regions with high dislocation densities and highly localized strain, and (2) the formation of dislocation walls that subsequently developed into low-angle sub-grain boundaries ($< 15^\circ$ misorientation).

Similarly, TEM of the dual-phase lamellar $\delta\text{-Ni}_3\text{Nb}/\mu\text{-Ni}_6\text{Nb}_7$ region (Fig. 3) shows the effects of plastic deformation on the microstructure. In Fig. 3A, B, and C, regions of the deformation zone were analyzed using STEM-EDS and STEM-HAADF. Chemical mapping was used to track $\delta\text{-Ni}_3\text{Nb}$ grains to ensure the darker regions in Fig. 3C were, in fact, an orientation change in the $\mu\text{-Ni}_6\text{Nb}_7$ grain. A higher magnification of the region within the dashed box in Fig. 3C is shown in Fig. 3D, where there is clear evidence of deformation twinning. The image reveals that regions of the lighter $\mu\text{-Ni}_6\text{Nb}_7$ grain appear darker after deformation. This change in contrast was found to be a result of {204} nanotwins, which appear confined to the $\mu\text{-Ni}_6\text{Nb}_7$ grain (Fig. 3E). Nanotwinning can be beneficial to mechanical properties, by confining dislocation motion, playing a similar role as grain boundaries in Hall-Petch type

Figure 2 Representative cross-sectional STEM images of nanoindentation-induced deformation zones within a large $\delta\text{-Ni}_3\text{Nb}$ phase. **A** High-angle annular dark-field (HAADF) image and **B** bright field (BF) image of dashed box shown in (A).



deformation twinning in nanostructured two-phase region

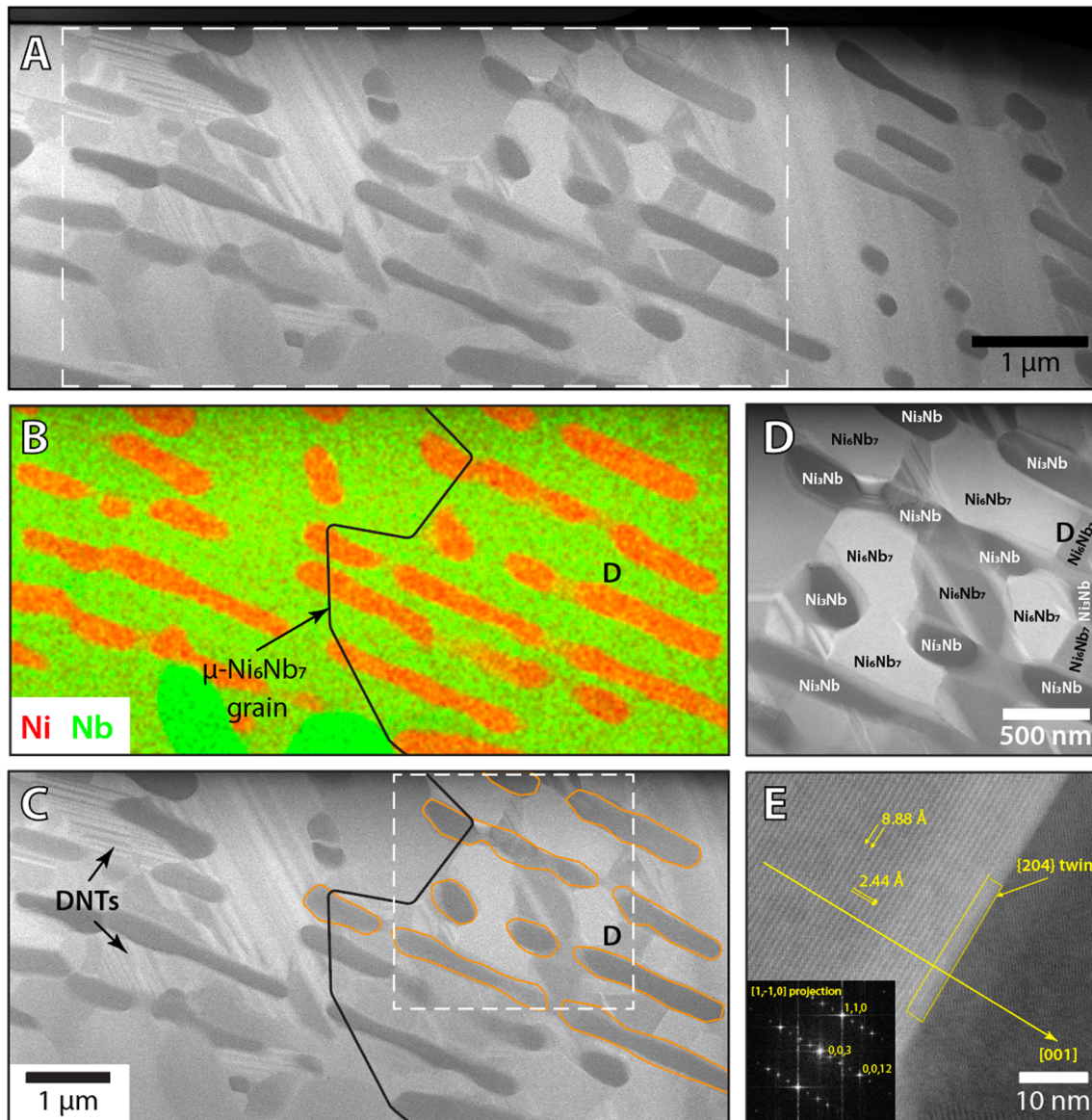


Figure 3 Cross-sectional STEM images of nanoindentation-induced deformation zones within δ - $\text{Ni}_3\text{Nb}/\mu$ - Ni_6Nb_7 lamellar phase. **A** STEM-HAADF low magnification image of deformed region. **B** STEM-EDS chemical map with outline of large μ - Ni_6Nb_7 grain boundary. Orange and green coloring corresponds to δ - Ni_3Nb and μ - Ni_6Nb_7 regions, respectively. **C** Corresponding STEM-HAADF image highlighting deformation nanotwins (DNTs) and guidelines (in orange) of δ - Ni_3Nb phase

strengthening and providing low energy boundaries that are thermally and mechanically stable [13, 62]. Additionally, the presence of impenetrable nanoprecipitates could aid in delocalizing slip and nanotwin pathways [63], leading to enhanced ductility. While the large δ - Ni_3Nb grains showed evidence of shear

from EDS analysis. The differences in contrast of the μ - Ni_6Nb_7 grain is indicative of an orientation change. **D** STEM-HAADF magnification of boxed region shown in (C), where each grain is labeled and, by the contrast, DNTs appear to be confined to the μ - Ni_6Nb_7 phase. **E** High-resolution STEM-HAADF along with FFT pattern from the left side of the grain (inset) in the $[1, -1, 0]$ zone axis.

banding, we find that the δ - Ni_3Nb grains in the dual-phase region remain largely undeformed, and the much larger grains of μ - Ni_6Nb_7 accommodate the bulk of the deformation (discussed in detail below).

The μ - Ni_6Nb_7 phase crystallizes into a rhombohedral lattice, forming a hexagonal unit cell. Others

have shown that plastic deformation of the μ -Ni₆Nb₇ phase is mediated by synchroshear, where the μ phase can be described by stacking of MgCu₂-type Laves and Zr₄Al₃-type layers as its building blocks [24, 25]. More generally, deformation-induced twin nucleation and growth have been well documented for purely hexagonal close-packed (HCP) metals, such as Mg and Ti [64–67]. In HCP structures, twinning acts simultaneously with slip and the preferred slip and twin planes do not coincide [68]. Therefore, slip/interface interactions can either completely block dislocation motion or induce non-planar reactions of lattice dislocations at the intersection site into twinning partials suitable for forming twins [69]. The nanoscale δ -Ni₃Nb inclusions could act as twin nucleation sites, given that twins are preferentially emitted from high-energy interfaces like grain boundaries and bimetal interfaces [64]. Generally, twinning is preferred at the more defective interfaces and geometrically well aligned slip and twin systems across the interface. In the present case, dislocations in the matrix that meets these interfaces on one side, which could dissociate and trigger the formation of twin embryos and twin dislocations to form on the other side [70]. With the generally limited slip system availability in intermetallics, twinning is likely the most energetically favorable route to accommodate plasticity up to 400 °C (Fig. 1E) and responsible for the high hardness over this temperature range. As in pure HCP metals, while for elevated temperatures, diffusion-mediated and/or multi-slip processes, including possibly higher-order planes, dominate over twinning, deformation twinning can still occur [71]. Room-temperature mechanical twinning has been observed in ordered Ti–Al alloys, and the addition of Mn to Ti–Al was found to promote deformation twinning [72]. Specifically, interactions among superdislocations [73] were shown to be the dominant deformation mechanism in the Ti–Al system, whereas in Ti–Al–Mn, deformation twinning became more favorable due to the decrease in stacking fault energy and as evidenced by the stabilization of twins/twin boundaries [72]. Ductility was also enhanced with the addition of Mn, and this was attributed to the transition to twinning as the dominant deformation mechanism [72].

Additionally, it has been observed across a wide range of metals that the twinning stress follows Hall–Petch behavior [74], increasing with decreasing grain size. As shown in twins in HCP metals, such as Mg

and Ti, a back stress is generated at the twin/grain boundary intersection, which increasing stunts twin expansion as grain size shrinks [75]. Deformation-induced twinning will more readily occur in the coarse grained μ -Ni₆Nb₇ where the stress required for twin formation is lower than that of the finer-grained δ -Ni₃Nb, though it is important to note that this relationship only holds with grain sizes above ~ 100 nm [64]. Although we were not able to systematically experimentally compare the strength of the two individual phases at their respective grain sizes, twinning was the only observed deformation mode immediately adjacent the indentation zone in the nanostructured two-phase region, and our simulation results (see Fig. 4) indicate that μ -Ni₆Nb₇ is stronger than δ -Ni₃Nb for equivalent grain sizes. Composition and process parameter tuning are a likely route for achieving similar properties in bulk, though this was beyond the scope of this project.

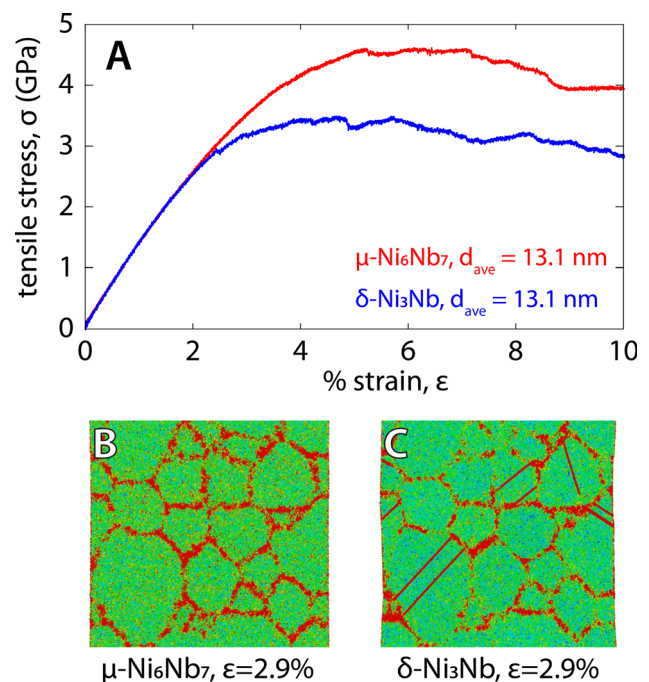


Figure 4 Summary of MD analysis on deformation behavior of μ -Ni₆Nb₇ and δ -Ni₃Nb phases with average grain size $d_{ave} = 13.1$ nm. **A** Stress–strain curves from uniaxial tension testing of μ -Ni₆Nb₇ and δ -Ni₃Nb cylindrical rods. **B** Snapshot of μ -Ni₆Nb₇ sample and **C** δ -Ni₃Nb sample at 2.9% strain. The color indicates the atomic strain with red indicating highest strain and blue and green indicating areas of low strain. Additional snapshots of the two phases at 2.9% (A, B) 4.0% (C, D) 6.4% (E, F), and 12% (G, H) strain are shown in Supplemental Figures I and II.

Computational modeling and simulations

A summary of MD simulations used to investigate the strength and deformation behavior of μ -Ni₆Nb₇, δ -Ni₃Nb phases is shown in Fig. 4. These simulations were designed to have identical microstructures across samples, allowing for comparisons across composition as a function of grain size. A series of uniaxial tensile tests on cylindrically shaped specimens were modeled with average grain size of 13.1 nm, and flow stress was computed from the strain-dependent average stress from 6 to 10% strain.

Figure 4A shows stress–strain curves for μ -Ni₆Nb₇ and δ -Ni₃Nb phases with $d_{\text{ave}} = 13.1$ nm. It is clear the Ni₃Nb phase is softer than that of Ni₆Nb₇, and the average flow strengths of μ -Ni₆Nb₇ and δ -Ni₃Nb are $\sigma_{\text{flow}} = 4.3$ GPa and $\sigma_{\text{flow}} = 3.1$ GPa, respectively. Maps of atomic strain at $\varepsilon = 2.9\%$ are shown in Fig. 4B and C. For the stronger μ -Ni₆Nb₇ phase, most of the strain is localized at grain boundaries, a characteristic of intergranular deformation (Fig. 4B). Conversely, δ -Ni₃Nb strain was primarily intragranular, localized within grains in the form of slip bands, confined to glide planes, indicating dislocation-mediated plasticity as the dominant mode of deformation [76, 77] (Fig. 4C). Literature on pure metals has shown that above $d_{\text{ave}} \cong 10$ nm, it is generally observed that dislocation activity is the dominant mechanism of plasticity, rather than grain boundary sliding [76–83]. While the grain size of MD and experimental investigations are not comparable, we note that slip bands were also experimentally observed in deformed δ -Ni₃Nb (Fig. 2A). Snapshots of deformation in the two phases at 2.9, 4.0, 6.4, and 12% strain are included in the Supplemental section. Some slip planes form within the μ -Ni₆Nb₇ grains at high strain, but far less than in the δ -Ni₃Nb phase under the same loading conditions.

Strengthening mechanisms

The MD results indicate deformation would take place preferentially in the softer δ -Ni₃Nb phase, seemingly contradicting the nanoindentation experiments (Fig. 1). However, as already mentioned, μ -Ni₆Nb₇ grains of the AM sample are much larger than the encapsulated δ -Ni₃Nb phase grains. A reasonable explanation for the discrepancy between MD and experiments is that due to Hall–Petch behavior [28], the nominally stronger μ -Ni₆Nb₇ phase

accommodates most of the deformation because of their far larger grain size. Additionally, the suppression of slip band formation in the nanoscale δ -Ni₃Nb phase and the promotion of deformation nanotwins in the coarse grained μ -Ni₆Nb₇ phase that was observed experimentally warrants a brief discussion. Because δ -Ni₃Nb nanograins are well-dispersed throughout the dual-phase lamellar region of the Ni–Nb sample, there exists a high density of bimetal interfaces that serve as a source of deformation twins [84, 85]. Studies have shown that deformation twinning is a direct consequence of the presence of a bimetal interface, where similar twinning behavior is not observed in individual constituents [64]. Secondly, in similar low symmetry metals, such as HCP, many studies have shown that deformation twinning becomes increasingly unlikely as grain size decreases [75, 86]. These are possible explanations as to why no deformation twinning was observed in the MD for purely μ -Ni₆Nb₇ nanograined rods (Fig. 4B). The nanoscale δ -Ni₃Nb inclusions are likely responsible for both the nucleation and growth of deformation nanotwins in the μ -Ni₆Nb₇ phase. The absence of slip band formation in the nanoscale δ -Ni₃Nb phase is also seen experimentally (Fig. 3), but not computationally (Fig. 4C). We offer a reasonable explanation based on the findings from a recent report [87] on an equiatomic CoCrNi medium-entropy alloy. Through a detailed investigation, the authors found that the presence of deformation nanotwins relieved high local stresses in the ternary alloy system, thereby suppressing or holding off severe plastic deformation. The mechanical energy absorption via deformation nanotwinning aids in the high fracture toughness ($K_c \approx 110$ MPa m^{1/2}) of CoCrNi. In the context of the Ni–Nb system, which we have shown previously [26] to have a reasonably high fracture toughness of $K_c \approx 70 - 90$ MPa m^{1/2}, it is possible that a similar mechanism is at play, where nanotwins, confined to the μ -Ni₆Nb₇ phase, thwart slip band formation in the δ -Ni₃Nb phase.

Concluding remarks

This work highlights the potential for rapid solidification and non-equilibrium processing pathways enabled by additive manufacturing to achieve a combination of high strength and ductility with microstructures that would be otherwise impractical

to achieve. Here, experimental and computational techniques were used to assess the strength of an AM-fabricated, near-eutectic, intermetallic of Ni_{59.5}-Nb_{40.5}. This study revealed a dual-phase lamellar region with high hardness, approaching a maximum value near $H \cong 17$ GPa. As evidenced by cross-sectional STEM, plasticity was predominantly accommodated by deformation twinning. It is proposed that the nanostructured δ -Ni₃Nb cells within the coarser grained μ -Ni₆Nb₇ matrix act as twin nucleation sites, with deformation twinning preferred over slip due to the limited number of available slip systems in intermetallic compounds in general. High-temperature nanoindentation testing revealed a retention of strength up to 400 °C, followed by a significant softening at about half of the melting temperature. This phase- and temperature-dependent study highlights the untapped potential enabled by non-traditional combinations of materials and processing/characterization tools.

Data and code availability

Measured data (indentation, etc.) available upon request.

Acknowledgements

This work was funded by the Laboratory Directed Research and Development program at Sandia National Laboratories, a multi-mission laboratory managed and operated by National Technology and Engineering Solutions of Sandia, LLC., a wholly owned subsidiary of Honeywell International, Inc., for the U.S. Department of Energy's National Nuclear Security Administration under contract DE-NA0003525. F.W.D. was supported by the Center for Integrated Nanotechnologies, a Department of Energy office of Basic Energy Sciences user facility. I.J.B. gratefully acknowledges support from the Office of Naval Research under contract N00014-21-1-2536. Any subjective views or opinions that might be expressed in the paper do not necessarily represent the views of the U.S. Department of Energy or the United States Government. The authors acknowledge Raymond Puckett at Sandia for conducting the AM processing experiments.

Declarations

Conflict of interest None of the authors have conflict(s) of interest to report.

Ethical approval Not applicable.

Supplementary Information: The online version contains supplementary material available at <http://doi.org/10.1007/s10853-023-08636-8>.

References

- [1] Perepezko JH (2009) The Hotter the engine, the better. *Science* (1979) 326:1068–1069. <https://doi.org/10.1126/science.1179327>
- [2] Frazier WE (2014) Metal additive manufacturing: a review. *J Mater Eng Perform* 23:1917–1928. <https://doi.org/10.1007/s11665-014-0958-z>
- [3] Lewandowski JJ, Seifi M (2016) Metal Additive manufacturing: a review of mechanical properties. *Annu Rev Mater Res* 46:151–186. <https://doi.org/10.1146/annurev-matsci-070115-032024>
- [4] Chen S, Tong Y, Liaw PK (2018) Additive manufacturing of high-entropy alloys: a review. *Entropy*. <https://doi.org/10.3390/e20120937>
- [5] Agrawal P, Thapliyal S, Nene SS et al (2020) Excellent strength-ductility synergy in metastable high entropy alloy by laser powder bed additive manufacturing. *Addit Manuf* 32:101098. <https://doi.org/10.1016/j.addma.2020.101098>
- [6] Babuska TF, Wilson MA, Johnson KL et al (2019) Achieving high strength and ductility in traditionally brittle soft magnetic intermetallics via additive manufacturing. *Acta Mater*. <https://doi.org/10.1016/j.actamat.2019.08.044>
- [7] Gorsse S, Hutchinson C, Gouné M, Banerjee R (2017) Additive manufacturing of metals: a brief review of the characteristic microstructures and properties of steels, Ti-6Al-4V and high-entropy alloys. *Sci Technol Adv Mater* 18:584–610. <https://doi.org/10.1080/14686996.2017.1361305>
- [8] de Cooman BC, Kwon O, Chin K-G (2012) State-of-the-knowledge on TWIP steel. *Mater Sci Technol* 28:513–527
- [9] de Cooman BC, Estrin Y, Kim SK (2018) Twinning-induced plasticity (TWIP) steels. *Acta Mater* 142:283–362
- [10] Deng Y, Tasan CC, Pradeep KG et al (2015) Design of a twinning-induced plasticity high entropy alloy. *Acta Mater* 94:124–133. <https://doi.org/10.1016/j.actamat.2015.04.014>
- [11] Asaro RJ, Suresh S (2005) Mechanistic models for the activation volume and rate sensitivity in metals with

- nanocrystalline grains and nano-scale twins. *Acta Mater* 53:3369–3382
- [12] Ding Q, Bei H, Wei X et al (2021) Nano-twin-induced exceptionally superior cryogenic mechanical properties of a Ni-based GH3536 (Hastelloy X) superalloy. *Mater Today Nano* 14:100110. <https://doi.org/10.1016/j.mtnano.2021.100110>
- [13] Ren L, Xiao W, Ma C et al (2018) Development of a high strength and high ductility near β -Ti alloy with twinning induced plasticity effect. *Scr Mater* 156:47–50. <https://doi.org/10.1016/j.scriptamat.2018.07.012>
- [14] Ding ZY, He QF, Chung D, Yang Y (2020) Evading brittle fracture in submicron-sized high entropy intermetallics in dual-phase eutectic microstructure. *Scr Mater* 187:280–284. <https://doi.org/10.1016/j.scriptamat.2020.06.032>
- [15] Gschneidner K, Russell A, Pecharsky A et al (2003) A family of ductile intermetallic compounds. *Nat Mater* 2:587–591
- [16] Yang T, Zhao YL, Tong Y et al (1979) (2018) Multicomponent intermetallic nanoparticles and superb mechanical behaviors of complex alloys. *Science* 362:933–937
- [17] Liu CT, Maziasz PJ, Wright JL (1996) Key microstructures controlling the mechanical properties of two-phase TiAl alloys with lamellar structures. *MRS Online Proc Lib (OPL)* 460
- [18] Jiao ZB, Luan JH, Liu CT (2016) Strategies for improving ductility of ordered intermetallics. *Prog Nat Sci: Mater Int* 26:1–12. <https://doi.org/10.1016/j.pnsc.2016.01.014>
- [19] Potnis G, Goswami D, Das J (2023) Twinning mediated plasticity in high entropy $\text{CoCr}_{1.3}\text{FeNi}_{0.7}\text{MnNb}_x$ ($x=0.3, 0.367, 0.4$) ultrafine lamellar eutectic by tuning stacking fault energy. *Scr Mater* 227:115271
- [20] Zhang Y, Li J, Wang X et al (2019) The interaction and migration of deformation twin in an eutectic high-entropy alloy $\text{AlCoCrFeNi}_{2.1}$. *J Mater Sci Technol* 35:902–906
- [21] Sundararaman M, Mukhopadhyay P, Banerjee S (1988) Precipitation of the δ -Ni₃Nb phase in two nickel base superalloys. *Metall Trans A* 19:453–465
- [22] Wu Y, Li S, Kang M et al (2019) Slip and fracture behavior of δ -Ni₃Nb plates in a polycrystalline nickel-based superalloy during fatigue. *Scr Mater* 171:36–41. <https://doi.org/10.1016/j.scriptamat.2019.06.013>
- [23] Karthik GM, Asghari-Rad P, Sathiyamoorthi P et al (2021) Architected multi-metal CoCrFeMnNi -Inconel 718 lamellar composite by high-pressure torsion. *Scr Mater* 195:113722
- [24] Schröders S, Sandlöbes S, Berkels B, Korte-Kerzel S (2019) On the structure of defects in the Fe 7 Mo 6 μ -Phase. *Acta Mater* 167:257–266. <https://doi.org/10.1016/j.actamat.2019.01.045>
- [25] Cheng Y, Wang G, Liu J, He L (2021) Atomic configurations of planar defects in μ phase in Ni-based superalloys. *Scr Mater* 193:27–32. <https://doi.org/10.1016/j.scriptamat.2020.09.045>
- [26] Jones MR, DelRio FW, Pegues JW et al (2021) Additive manufacturing of high-strength multiphase nanostructures in the binary Ni–Nb system for the discovery of new types of superalloys. *J Mater Res* 36:3167–3181. <https://doi.org/10.1557/s43578-021-00290-7>
- [27] Shaw LL, Ortiz AL, Villegas JC (2008) Hall–Petch relationship in a nanotwinned nickel alloy. *Scr Mater* 58:951–954. <https://doi.org/10.1016/j.scriptamat.2008.01.025>
- [28] Cordero ZC, Knight BE, Schuh CA (2016) Six decades of the Hall–Petch effect: a survey of grain-size strengthening studies on pure metals. *Int Mater Rev* 61:495–512. <https://doi.org/10.1080/09506608.2016.1191808>
- [29] Kozar RW, Suzuki A, Milligan WW et al (2009) Strengthening mechanisms in polycrystalline multimodal nickel-base superalloys. *Metall and Mater Trans A* 40:1588–1603
- [30] Chandross M, Argibay N (2020) Ultimate strength of metals. *Phys Rev Lett* 124:125501. <https://doi.org/10.1103/PhysRevLett.124.125501>
- [31] George EP, Raabe D, Ritchie RO (2019) High-entropy alloys. *Nat Rev Mater* 4:515–534. <https://doi.org/10.1038/s41578-019-0121-4>
- [32] Miracle DB, Senkov ON (2017) A critical review of high entropy alloys and related concepts. *Acta Mater* 122:448–511. <https://doi.org/10.1016/j.actamat.2016.08.081>
- [33] Kustas AB, Susan DF, Johnson KL et al (2018) Characterization of the Fe–Co–1.5V soft ferromagnetic alloy processed by laser engineered net shaping (LENS). *Addit Manuf* 21:41–52
- [34] Tukey J (1953) Multiple comparisons. *J Am Stat Assoc* 48:624–625
- [35] Plimpton S (1995) Fast parallel algorithms for short-range molecular dynamics. *J Comput Phys* 117:1–19
- [36] Thompson AP, Aktulga HM, Berger R et al (2022) LAMMPS—a flexible simulation tool for particle-based materials modeling at the atomic, meso, and continuum scales. *Comput Phys Commun* 271:108171
- [37] Zhang Y, Ashcraft R, Mendeleev MI et al (2016) Experimental and molecular dynamics simulation study of structure of liquid and amorphous $\text{Ni}_{62}\text{Nb}_{38}$ alloy. *J Chem Phys* 145:204505
- [38] Anderson MP, Srolovitz DJ, Grest GS, Sahni PS (1984) Computer simulation of grain growth—I. *Kinet Acta Metall* 32:783–791
- [39] Holm EA, Glazier JA, Srolovitz DJ, Grest GS (1991) Effects of lattice anisotropy and temperature on domain growth in

- the two-dimensional Potts model. *Phys Rev A (Coll Park)* 43:2662–2668
- [40] Plimpton S, Corbett Battaile MC, Holm L, et al (2009) Crossing the mesoscale no-man's land via parallel kinetic Monte Carlo, Sandia Report SAND2009-6226
- [41] Espinosa HD, Prorok BC, Peng B (2004) Plasticity size effects in free-standing submicron polycrystalline FCC films subjected to pure tension. *J Mech Phys Solids* 52:667–689. <https://doi.org/10.1016/j.jmps.2003.07.001>
- [42] Horstemeyer MF, Baskes MI, Plimpton SJ (2001) Length scale and time scale effects on the plastic flow of fcc metals. *Acta Mater* 49:4363–4374
- [43] Elmustafa AA, Stone DS (2003) Nanoindentation and the indentation size effect: kinetics of deformation and strain gradient plasticity. *J Mech Phys Solids* 51:357–381. [https://doi.org/10.1016/S0022-5096\(02\)00033-9](https://doi.org/10.1016/S0022-5096(02)00033-9)
- [44] Nix WD, Gao H (1998) Indentation size effects in crystalline materials: a law for strain gradient plasticity. *J Mech Phys Solids* 46:411–425. [https://doi.org/10.1016/S0022-5096\(97\)00086-0](https://doi.org/10.1016/S0022-5096(97)00086-0)
- [45] Pharr GM, Herbert EG, Gao Y (2010) The indentation size effect: a critical examination of experimental observations and mechanistic interpretations. *Annu Rev Mater Res* 40:271–292
- [46] Uchic MD, Dimiduk DM, Florando JN, Nix WD (2004) Sample dimensions influence strength and crystal plasticity. *Science* (1979) 305:986–989
- [47] Li TL, Bei H, Morris JR et al (2012) Scale effects in convoluted thermal/spatial statistics of plasticity initiation in small stressed volumes during nanoindentation. *Mater Sci Technol* 28:1055–1059. <https://doi.org/10.1179/1743284712Y.0000000007>
- [48] Silva CC, De Albuquerque VHC, Miná EM et al (2018) Mechanical properties and microstructural characterization of aged nickel-based alloy 625 weld metal. *Metall Mater Trans A* 49:1653–1673
- [49] Belan J, Vaško A, Kuchariková L et al (2018) The high-temperature loading influence on orthorhombic Ni_3Nb DO δ phase formation and its effect on fatigue lifetime in alloy 718. *Manuf Technol* 18:875–882
- [50] Fukuchi M, Watanabe K (1986) On the plastic deformation of a Ni_3Nb single crystal. *Trans Jpn Inst Metals* 27:434–440
- [51] Hagihara K, Nakano T, Umakoshi Y (2000) Plastic deformation behaviour and operative slip systems in Ni_3Nb single crystals. *Acta Mater* 48:1469–1480. [https://doi.org/10.1016/S1359-6454\(99\)00447-4](https://doi.org/10.1016/S1359-6454(99)00447-4)
- [52] Afonso CRM, Martinez-Orozco K, Amigó V et al (2020) Characterization, corrosion resistance and hardness of rapidly solidified Ni–Nb alloys. *J Alloys Compd* 829:154529. <https://doi.org/10.1016/j.jallcom.2020.154529>
- [53] Ezugwu EO, Bonney J, Yamane Y (2003) An overview of the machinability of aeroengine alloys. *J Mater Process Technol* 134:233–253
- [54] Bolcavage A, Kattner UR (1996) A reassessment of the calculated Ni–Nb phase diagram. *J Phase Equilib* 17:92–100. <https://doi.org/10.1007/BF02665782>
- [55] Wang H, Dhiman A, Ostergaard HE et al (2019) Nanoindentation based properties of Inconel 718 at elevated temperatures: a comparison of conventional versus additively manufactured samples. *Int J Plast* 120:380–394
- [56] Feng K, Chen Y, Deng P et al (2017) Improved high-temperature hardness and wear resistance of Inconel 625 coatings fabricated by laser cladding. *J Mater Process Technol* 243:82–91
- [57] Korznikov AV, Tram G, Dimitrov O et al (2001) The mechanism of nanocrystalline structure formation in Ni_3Al during severe plastic deformation. *Acta Mater* 49:663–671
- [58] Fecht H-J (1995) Nanostructure formation by mechanical attrition. *Nanostruct Mater* 6:33–42
- [59] Lu JZ, Zhong JW, Luo KY et al (2011) Micro-structural strengthening mechanism of multiple laser shock processing impacts on AISI 8620 steel. *Mater Sci Eng: A* 528:6128–6133. <https://doi.org/10.1016/j.msea.2011.04.018>
- [60] Ren XD, Zhou WF, Liu FF et al (2016) Microstructure evolution and grain refinement of Ti–Al–4V alloy by laser shock processing. *Appl Surf Sci* 363:44–49. <https://doi.org/10.1016/j.apsusc.2015.11.192>
- [61] Hong CS, Tao NR, Huang X, Lu K (2010) Nucleation and thickening of shear bands in nano-scale twin/matrix lamellae of a Cu–Al alloy processed by dynamic plastic deformation. *Acta Mater* 58:3103–3116
- [62] Huang CX, Hu WP, Wang QY et al (2015) An ideal ultrafine-grained structure for high strength and high ductility. *Mater Res Lett* 3:88–94. <https://doi.org/10.1080/21663831.2014.968680>
- [63] Wu H, Fan G (2020) An overview of tailoring strain delocalization for strength-ductility synergy. *Prog Mater Sci* 113:100675. <https://doi.org/10.1016/j.pmatsci.2020.100675>
- [64] Beyerlein IJ, Zhang X, Misra A (2014) Growth twins and deformation twins in metals. *Annu Rev Mater Res* 44:329–363
- [65] Jiang L, Kumar MA, Beyerlein IJ et al (2019) Twin formation from a twin boundary in Mg during in-situ nanomechanical testing. *Mater Sci Eng, A* 759:142–153
- [66] Arul Kumar M, Beyerlein IJ, Tome CN (2016) Grain size constraints on twin expansion in hexagonal close packed crystals. *J Appl Phys* 120:155105
- [67] Jiang L, Gong M, Wang J et al (2022) Visualization and validation of twin nucleation and early-stage growth in magnesium. *Nat Commun* 13:1–11

- [68] Yoo MH (1969) Interaction of slip dislocations with twins in HCP metals. Oak Ridge National Lab, Tenn
- [69] Ahmadikia B, Wang L, Kumar MA, Beyerlein IJ (2023) Grain boundary slip–twin transmission in titanium. *Acta Mater* 244:118556
- [70] Wang J, Beyerlein IJ, Tomé CN (2014) Reactions of lattice dislocations with grain boundaries in Mg: implications on the micro scale from atomic-scale calculations. *Int J Plast* 56:156–172
- [71] Knezevic M, Beyerlein IJ, Nizolek T et al (2013) Anomalous basal slip activity in zirconium under high-strain deformation. *Mater Res Lett* 1:133–140
- [72] Kim Y-W (1994) Ordered intermetallic alloys, part III: gamma titanium aluminides. *Jom* 46:30–39
- [73] Hanamura T, Uemori R, Tanino M (1988) Mechanism of plastic deformation of Mn-added TiAl L 10-type intermetallic compound. *J Mater Res* 3:656–664
- [74] Kovarik L, Unocic RR, Li J et al (2009) Microtwinning and other shearing mechanisms at intermediate temperatures in Ni-based superalloys. *Prog Mater Sci* 54:839–873. <https://doi.org/10.1016/j.pmatsci.2009.03.010>
- [75] Kumar MA, Beyerlein IJ (2020) Influence of plastic properties on the grain size effect on twinning in Ti and Mg. *Mater Sci Eng A* 771:138644
- [76] Hugo RC, Kung HW, Knapp JA, Follstaedt DM (2003) *Acta Mater* 51:1937–1943
- [77] Jakob S, JK W (2003) A maximum in the strength of nanocrystalline copper. *Science* (1979) 301:1357–1359. <https://doi.org/10.1126/science.1086636>
- [78] Yip S (2004) Mapping plasticity. *Nat Mater* 3:11–12
- [79] Zhang T, Zhou K, Chen ZQ (2015) Strain rate effect on plastic deformation of nanocrystalline copper investigated by molecular dynamics. *Mater Sci Eng A* 648:23–30
- [80] Schiøtz J, di Tolla FD, Jacobsen KW (1998) Softening of nanocrystalline metals at very small grain sizes. *Nature* 391:561–563
- [81] Yamakov V, Wolf D, Phillpot SR, Mukherjee AK, Gleiter H (2002) *Nat Mater* 1:45–49
- [82] Gertsman VY, Hoffmann M, Gleiter H, Birringer R (1994) The study of grain size dependence of yield stress of copper for a wide grain size range. *Acta Metall Mater* 42:3539–3544
- [83] Liu J, Fan X, Zheng W et al (2020) Nanocrystalline gold with small size: inverse Hall–Petch between mixed regime and super-soft regime. *Phil Mag* 100:2335–2351
- [84] McCabe RJ, Beyerlein IJ, Carpenter JS, Mara NA (2014) The critical role of grain orientation and applied stress in nanoscale twinning. *Nat Commun* 5:1–7
- [85] Beyerlein IJ, Wang J, Kang K et al (2013) Twinability of bimetal interfaces in nanostructured composites. *Mater Res Lett* 1:89–95
- [86] Kumar MA, Beyerlein IJ (2020) Local microstructure and micromechanical stress evolution during deformation twinning in hexagonal polycrystals. *J Mater Res* 35:217–241
- [87] Wu X, Yang M, Jiang P et al (2020) Deformation nanotwins suppress shear banding during impact test of CrCoNi medium-entropy alloy. *Scr Mater* 178:452–456. <https://doi.org/10.1016/j.scriptamat.2019.12.017>

Publisher’s Note Springer Nature remains neutral with regard to jurisdictional claims in published maps and institutional affiliations.

Springer Nature or its licensor (e.g. a society or other partner) holds exclusive rights to this article under a publishing agreement with the author(s) or other rightsholder(s); author self-archiving of the accepted manuscript version of this article is solely governed by the terms of such publishing agreement and applicable law.